Journal of the Mechanics and Physics of Solids 61 (2013) 145–160

Contents lists available at SciVerse ScienceDirect

Journal of the Mechanics and Physics of Solids

journal homepage: www.elsevier.com/locate/jmps

Optimal overlap length in staggered architecture composites under dynamic loading conditions

Abhishek Dutta [a], Srinivasan Arjun Tekalur [a,*], Milan Miklavcic [b]

[a] Department of Mechanical Engineering, Michigan State University, East Lansing, MI 48824, USA
[b] Department of Mathematics, Michigan State University, East Lansing, MI 48823, USA

ARTICLE INFO

Article history:
Received 11 May 2012
Received in revised form
8 August 2012
Accepted 14 August 2012
Available online 28 August 2012

Keywords:
Biological material
Microstructures
Shear transfer
Analytic functions

ABSTRACT

Hybrid staggered architecture composites, like nacre and bone, are known for two discernible aspects: superior strength and synergistic toughness. What is lacking is the scientific rationale proving suitability of these materials under impact/time dependent loading. The current investigation aims to address the structure-property correlationship of these materials by development of an analytical model under dynamic rates of loading. Existing literature studies address behavior of staggered materials under quasi-static loading conditions. Critical overlap length was computed for three natural composites-nacre, spider-silk and, collagen in bone/tendon, and showed reasonable agreement with experimental data. Applicability of the analytical approach to predict lap-joint strength has been briefly discussed and quantified against experimental data. Choice of nanometer sized building blocks in natural composites has been addressed and explained from shear transfer efficiency point of view. The potentiality of these composites for use as biomimetic protective material under impact loading has been addressed as well.

1. Introduction

Nacre refers to the inner shining layer in seashells. Microstructure of nacre reveals the existence of mineral tablets in a soft polymeric matrix in a brick-and-mortar structural arrangement (Jackson et al., 1988; Sarikaya et al., 1990). Two of the most discerning aspects of nacre are exhibition of superior strength and synergistic toughness (Barthelat and Espinosa, 2007a; Jackson et al., 1988; Kessler et al., 1996; Kamat et al., 2000; Menig et al., 2000, 2001; Sarikaya et al., 1990). Multifarious factors contribute to toughening mechanisms, namely tablet pull-out (Jackson et al., 1988), crack deflection by the polymeric matrix (Menig et al., 2000), platelet interlocks (Katti et al., 2005), presence of nanoasperities (Evans et al., 2001; Wang et al., 2001), diffusive tablet sliding (Barthelat and Espinosa, 2007a) arising from tablet waviness, aragonite bridge reinforcements at interface (Song et al., 2003), and re-locking of tablets (Meyers et al., 2008) due to persistent contact of broken aragonite bridges, all contribute to interfacial strengthening and thereby, superior fracture resistance.

So far, literature studies have addressed the interdependence of material properties and geometrical parameters on mechanical behavior of the staggered architecture materials under quasi-static loading conditions. Analytical model proposed by Jager and Fratzl (2000) estimated the maximum stress and strain of the composite, by advancing previously established models for the mechanical properties of mineralized collagen fibrils (Wagner and Weiner, 1992) by setting forth inorganic crystals in a staggered arrangement in agreement with the distribution of gaps in the collagen fibril

* Corresponding author. Tel.: +1 517 884 1608; fax: +1 517 884 1601.
E-mail address: tsarjun@egr.msu.edu (S.A. Tekalur).

0022-5096/$ - see front matter © 2012 Elsevier Ltd. All rights reserved.
http://dx.doi.org/10.1016/j.jmps.2012.08.005

(Hulmes et al., 1995; Landis, 1995; Veis and Sabsay, 1987). Micromechanical model developed by Kotha et al. (2000) derived axial and shear stress distribution in platelets on the assumption of a fundamental basis that the load carried by the platelets remains constant and inter-platelet load transfer occurs by shear. Tension-shear-chain (TSC) model postulated by Gao et al. (2003) established the relationship between stiffness, aspect ratio of minerals, mineral volume fraction and material properties. Additionally, a critical overlap length, using Griffith's fracture criterion, was developed which attributed to the existence of an optimal aspect ratio of mineral crystals in biological composites. Shuchun and Yueguang (2007) used shear-lag model to study the interdependence of the overall elastic modulus and number of hierarchical levels in bone-like materials, and compared their results against TSC model and finite element simulations. Investigations by Chen et al. (2009) were directed towards understanding characteristic length for efficient stress transfer in staggered biocomposites via derivation of an analytical model followed by numerical simulations. Zhang et al. (2010) employed homogenization method to investigate the effect of platelet distribution (regular, stairwise, random), in staggered architecture materials, on the stiffness, strength, failure strain and energy storage capacity. Zhang et al. (2011) developed a quasi-self-similar hierarchical model to investigate the cause responsible for determination and existence of optimal number of hierarchical levels in staggered architecture materials, for varying mineral content, to obtain maximal toughness. Liu et al. (2011) used perturbation method to obtain analytical expressions for displacement and stress fields in the staggered nanocomposite structure, under quasi-static loading conditions, when subjected to uniaxial tension. Recently, Wei et al. (2012) laid down a criterion which reveals the existence of a unique overlap length in biological composites that contributes to an optimization on both, strength and toughness fronts.

Resistance to crushing against crustacean predators is an integral part of shell evolution. Shell breaking methods by predators is representative of a dynamic loading event. It has been observed that under high strain-rates (using a Split-Hopkinson pressure bar (SHPB)), nacre exhibits superior damage tolerance and elevated fracture strength (Huang et al., 2011). This behavior has been attributed to, based on electron microscopic analyses, on the existence of phenomenon's like partial dislocation emission and the onset of deformation twinning within the mineral crystals. However, minimal literature exists which addresses analytically the factors responsible for this behavior under dynamic rates of loading.

The following sections attempt to investigate and answer the following questions with regards to composites having staggered microstructure as its most elementary level of architecture under impact loading conditions. (1) Does there exist a structure-property correlationship for these materials under dynamic events? (2) Critical overlap length exists under quasi-static loading conditions which optimizes both strength and stiffness; is there any associated critical overlap length involved in load transfer mechanism between the adjacent reinforcements in dynamic regime? (3) As had been postulated by Gao et al. (2003), building blocks in biological composites are at nanometer scales under quasi-static loading conditions; is the same argument true under impact loading? In order to address these questions, we based our analyses in the following manner: (a) Analytical model development for staggered microstructural materials under time dependent loading considering linear elastic behavior, (b) identification of the critical overlap length criterion involved in these events, (c) predicting overlap lengths for other biocomposites exhibiting staggered microstructure as its most elementary level of architecture, for example nacre, spider-silk and collagen in bone/tendon, (d) predicting & validating the joint strength, using the analytical model, of aluminum-loctite lap joint under impact loading using SHPB (Sen et al., 2011), (e) provide an explanation, based on the analytical model, for superior damage tolerance and elevated dynamic compressive strength of nacre, and (f) insights into the effect of loading rate.

2. Mathematical formulation

We begin our analysis by taking into consideration the simplified 2D unit cell, as shown in Fig. 1(a), and by employing 'shear-lag theory' (Volkersen, 1938).

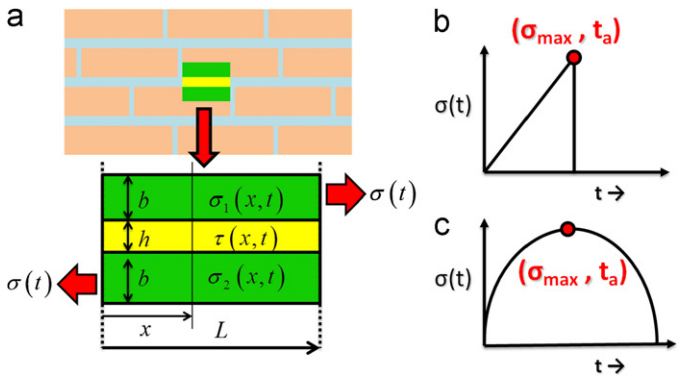

Fig. 1. (a) Schematic of brick-and-mortar microstructure identifying the overlap region; Representative loading pulses obtained from SHPB experiments: (b) triangular pulse and (c) half-sinusoidal pulse.

Applying force equilibrium to the upper and lower ceramic bricks, we obtain

$$\frac{\partial \sigma_1}{\partial x} - \frac{\tau}{b} = \rho \frac{\partial^2 u_1}{\partial t^2} \tag{1}$$

$$\frac{\partial \sigma_2}{\partial x} + \frac{\tau}{b} = \rho \frac{\partial^2 u_2}{\partial t^2} \tag{2}$$

where, $\sigma_1 \equiv \sigma_1(x,t)$ and $\sigma_2 \equiv \sigma_2(x,t)$ denotes the normal stress developed in the upper and lower ceramic bricks, τ denotes the shear stress developed in the polymer, b denotes half the ceramic brick width and h, the polymeric thickness. Assuming a state of pure shear in the polymer, we have $\tau = G(u_1 - u_2/h)$ where, $u_1 \equiv u_1(x,t)$, $u_2 \equiv u_2(x,t)$ denotes in-plane displacement of the upper and lower ceramic bricks, respectively, and G denotes the shear modulus of the polymer. Assuming linear elastic behavior of the ceramic bricks, i.e., $\sigma = E\partial u/\partial x$, where E denotes Young's modulus of elasticity of the ceramic, Eqs. (1) and (2) can we rewritten as Eqs. (3) and (4), to obtain the governing differential equation of the system, given by

$$\frac{\partial^2 u_1}{\partial x^2} - \frac{G}{Ebh}(u_1 - u_2) = \frac{1}{c^2}\frac{\partial^2 u_1}{\partial t^2} \tag{3}$$

$$\frac{\partial^2 u_2}{\partial x^2} + \frac{G}{Ebh}(u_1 - u_2) = \frac{1}{c^2}\frac{\partial^2 u_2}{\partial t^2} \tag{4}$$

where $c = \sqrt{E/\rho}$denotes the wave velocity through the ceramic and, ρ denotes the density of the ceramic. The boundary conditions of the system are given by

$$\sigma_2(0,t) = \sigma(t) \Rightarrow \left.\frac{\partial u_2}{\partial x}\right|_{(0,t)} = \frac{\sigma(t)}{E} \tag{5}$$

$$\sigma_1(0,t) = 0 \Rightarrow \left.\frac{\partial u_1}{\partial x}\right|_{(0,t)} = 0 \tag{6}$$

$$\sigma_2(L,t) = 0 \Rightarrow \left.\frac{\partial u_2}{\partial x}\right|_{(L,t)} = 0 \tag{7}$$

$$\sigma_1(L,t) = \sigma(t) \Rightarrow \left.\frac{\partial u_1}{\partial x}\right|_{(L,t)} = \frac{\sigma(t)}{E} \tag{8}$$

The initial conditions of the system are given by

$$u_1(x,0) = 0 \tag{9}$$

$$u_2(x,0) = 0 \tag{10}$$

$$\left.\frac{\partial u_1}{\partial t}\right|_{(x,0)} = 0 \tag{11}$$

$$\left.\frac{\partial u_2}{\partial t}\right|_{(x,0)} = 0 \tag{12}$$

We thus have coupled partial hyperbolic differential equations subjected to non-homogenous boundary conditions. Given the nature of the problem, we employed advanced separation of variables technique coupled with rearrangement of terms to obtain a closed-form solution for the displacements in the ceramic blocks.

We now introduce a variable, $u_4 \equiv u_4(x,t)$ which is defined as follows:

$$u_4(x,t) = u_1(x,t) - u_2(x,t) \tag{13}$$

Additionally, we define $u_4 \equiv u_4(x,t)$ in an alternative manner as follows:

$$u_4(x,t) = v(x,t) + w(x,t) \tag{14}$$

where $w(x,t)$ represents a smoothing function satisfying only the boundary conditions, i.e.,

$$\left.\frac{\partial w}{\partial x}\right|_{(0,t)} = -\frac{\sigma(t)}{E} \tag{15}$$

$$\left.\frac{\partial w}{\partial x}\right|_{(L,t)} = \frac{\sigma(t)}{E} \tag{16}$$

Subtracting Eq. (4) from Eq. (3) and substituting Eq. (14), we obtain another governing differential equation of the system, given by

$$\frac{\partial^2 v}{\partial x^2} - kv - \frac{1}{c^2}\frac{\partial^2 v}{\partial t^2} = -\frac{\partial^2 w}{\partial x^2} + kw + \frac{1}{c^2}\frac{\partial^2 w}{\partial t^2} \tag{17}$$

where, $k = 2G/Ebh$, and is subjected to boundary conditions and initial conditions, given by Eqs. (18)–(21), respectively.

$$\left.\frac{\partial v}{\partial x}\right|_{(0,t)} = 0 \tag{18}$$

$$\left.\frac{\partial v}{\partial x}\right|_{(L,t)} = 0 \tag{19}$$

$$v(x,0) = -w(x,0) \tag{20}$$

$$\left.\frac{\partial v}{\partial t}\right|_{(x,0)} = -\left.\frac{\partial w}{\partial t}\right|_{(x,0)} \tag{21}$$

Since boundary conditions are to be satisfied, choice of $w(x,t)$ is made on the basis of Neumann boundary conditions, and is thus represented by

$$w(x,t) = \frac{\sigma(t)}{E}\left(\frac{x^2}{L} - x\right) \tag{22}$$

Substituting Eq. (22) into right-hand side of Eq. (17), we thus have the following differential equation of the system, given by

$$\frac{\partial^2 v}{\partial x^2} - kv - \frac{1}{c^2}\frac{\partial^2 v}{\partial t^2} = p_4(x,t) = p_{04}(t) + \sum_{n \geq 1} p_{n4}(t)\cos\left(\frac{n\pi x}{L}\right) \tag{23}$$

where,

$$p_4(x,t) = \left[-\frac{2}{L} + k\left(\frac{x^2}{L} - x\right)\right]\frac{\sigma(t)}{E} + \frac{1}{c^2 E}\left(\frac{x^2}{L} - x\right)\frac{d^2\sigma(t)}{dt^2} \tag{24}$$

$$p_{04}(t) = \frac{1}{L}\int_{x=0}^{L} p_4(x,t)dx = -\left(\frac{12 + kL^2}{6EL}\right)\sigma(t) - \left(\frac{L}{6c^2 E}\right)\frac{d^2\sigma(t)}{dt^2} \tag{25}$$

$$p_{n4}(t) = \frac{2}{L}\int_{x=0}^{L} p_4(x,t)\cos\left(\frac{n\pi x}{L}\right)dx = \left(\frac{2LK}{E}\right)\left(\frac{1+\cos(n\pi)}{n^2\pi^2}\right)\sigma(t) + \left(\frac{2L}{c^2 E}\right)\left(\frac{1+\cos(n\pi)}{n^2\pi^2}\right)\frac{d^2\sigma(t)}{dt^2}, \quad n \geq 1 \tag{26}$$

Assume, $v(x,t) = X_4(x)T_4(t)$. The eigen values and functions are thus given by

$$\lambda_{n4} = \left(\frac{n\pi}{L}\right)^2, \quad n \geq 0 \tag{27}$$

$$X_{n4}(x) = \cos\left(\frac{n\pi x}{L}\right), \quad n \geq 0 \tag{28}$$

Hence, the formal solution of the problem is given by formal Fourier series, as

$$v(x,t) = \sum_{n \geq 0} T_{n4}(t)\cos\left(\frac{n\pi x}{L}\right) = T_{04}(t) + \sum_{n \geq 1} T_{n4}(t)\cos\left(\frac{n\pi x}{L}\right) \tag{29}$$

Substituting Eq. (29) into left-hand side of Eq. (23) and equating both sides, we get

$$\frac{d^2 T_{n4}}{dt^2} + \left[c^2\left\{k + \left(\frac{n\pi}{L}\right)^2\right\}\right]T_{n4} = -c^2 p_{n4}(t), \ n \geq 1 \tag{30}$$

$$\frac{d^2 T_{04}}{dt^2} + kc^2 T_{04} = -c^2 p_{04}(t) \tag{31}$$

The initial conditions, Eqs. (20) and (21), can be rewritten as follows:

$$v(x,0) = T_{04}(0) + \sum_{n \geq 1} T_{n4}(0)\cos\left(\frac{n\pi x}{L}\right) = -w(x,0) = -\left(\frac{x^2}{L} - x\right)\frac{\sigma(0)}{E}$$
$$\Rightarrow T_{04}(0) = \frac{L\sigma(0)}{6E}, \ T_{n4}(0) = -\frac{2L\sigma(0)}{E}\left(\frac{1+\cos(n\pi)}{n^2\pi^2}\right) \tag{32}$$

$$\left.\frac{\partial v}{\partial t}\right|_{(x,0)} = \frac{dT_{04}(0)}{dt} + \sum_{n\geq 1}\frac{dT_{n4}(0)}{dt}\cos\left(\frac{n\pi x}{L}\right) = -\left.\frac{\partial w}{\partial t}\right|_{(x,0)} = -\frac{1}{E}\frac{d\sigma(0)}{dt}\left(\frac{x^2}{L}-x\right) = q_4(x) = q_{04} + \sum_{n\geq 1} q_{n4}\cos\left(\frac{n\pi x}{L}\right)$$

$$\Rightarrow \frac{dT_{04}(0)}{dt} = q_{04} = \frac{1}{L}\int_{x=0}^{L} q_4(x)dx = \frac{L}{6E}\frac{d\sigma(0)}{dt}, \quad \text{and} \Rightarrow \frac{dT_{n4}(0)}{dt} = q_{n4} = \frac{2}{L}\int_{x=0}^{L} q_4(x)\cos\left(\frac{n\pi x}{L}\right)dx$$

$$= -\frac{2L}{E}\left(\frac{1+\cos(n\pi)}{n^2\pi^2}\right)\frac{d\sigma(0)}{dt}, \quad n\geq 1 \tag{33}$$

Eq. (30) can be rewritten as follows:

$$\frac{d^2T_{n4}}{dt^2} + e_{n4}^2 T_{n4} = -c^2 a_{n4}\left(\frac{k\sigma(t)}{E} + \frac{1}{c^2E}\frac{d^2\sigma(t)}{dt^2}\right), \quad n\geq 1 \tag{34}$$

where, $a_{n4}=2L(1+\cos(n\pi)/n^2\pi^2)$, and $e_{n4}=c\sqrt{k+(n\pi/L)^2}$. Eq. (34) can be rearranged further to obtain Eq. (35) as follows:

$$\left[\frac{d^2T_{n4}}{dt^2} + \frac{a_{n4}}{E}\frac{d^2\sigma(t)}{dt^2}\right] + e_{n4}^2\left[T_{n4} + \frac{a_{n4}}{E}\sigma(t)\right] = -\frac{c^2a_{n4}k\sigma(t)}{E} + \frac{e_{n4}^2a_{n4}\sigma(t)}{E} = \frac{a_{n4}}{E}\left(\frac{n\pi c}{L}\right)^2\sigma(t) \tag{35}$$

Eq. (35) can be written in a simplified manner to obtain Eq. (36) as follows:

$$\Rightarrow \frac{d^2y_4(t)}{dt^2} + e_{n4}^2 y_4(t) = g_4(t) \tag{36}$$

where,

$$y_4(t) = T_{n4} + \frac{a_{n4}}{E}\sigma(t), \quad \text{and} \quad g_4(t) = \frac{a_n}{E}\left(\frac{n\pi c}{L}\right)^2\sigma(t) \tag{37}$$

We use Laplace transform to solve Eq. (36). Let us denote $L\{y_4(t)\}=Y_4(s)$, and $L\{g_4(t)\}=G_4(s)$. Thus, we obtain

$$s^2Y_4(s) - sy_4(0) - \frac{dy_4(0)}{dt} + e_{n4}^2Y_4(s) = G_4(s)$$

$$\Rightarrow Y_4(s) = \left(\frac{s}{s^2+e_{n4}^2}\right)y_4(0) + \left(\frac{1}{s^2+e_{n4}^2}\right)\frac{dy_4(0)}{dt} + \left(\frac{1}{s^2+e_{n4}^2}\right)G_4(s)$$

$$\Rightarrow y_4(t) = y_4(0)\cos(e_{n4}t) + \frac{dy_4(0)}{dt}\frac{\sin(e_{n4}t)}{e_{n4}} + \int_{\tau=0}^{t}\frac{1}{e_{n4}}\sin(e_{n4}(t-\tau))g_4(\tau)d\tau \tag{38}$$

Note that,

$$y_4(0) = T_{n4}(0) + \tfrac{a_{n4}}{E}\sigma(0) = -\frac{2L\sigma(0)}{E}\left(\frac{1+\cos(n\pi)}{n^2\pi^2}\right) + \frac{2L\sigma(0)}{E}\left(\frac{1+\cos(n\pi)}{n^2\pi^2}\right) = 0, \text{ and}$$

$$\frac{dy_4(0)}{dt} = \frac{dT_{n4}(0)}{dt} + \frac{a_{n4}}{E}\frac{d\sigma(0)}{dt} = -\frac{2L}{E}\left(\frac{1+\cos(n\pi)}{n^2\pi^2}\right)\frac{d\sigma(0)}{dt} + \frac{2L}{E}\left(\frac{1+\cos(n\pi)}{n^2\pi^2}\right)\frac{d\sigma(0)}{dt} = 0 \tag{39}$$

and thus, using Eqs. (37)–(39), we finally obtain

$$T_{n4}(t) = -\frac{a_{n4}}{E}\sigma(t) + \frac{a_{n4}}{Ee_{n4}}\left(\frac{n\pi c}{L}\right)^2\int_{\tau=0}^{t}\sigma(\tau)\sin(e_{n4}(t-\tau))d\tau, \quad n\geq 1 \tag{40}$$

Lets us now solve Eq. (31). We proceed as follows. Eq. (31) can be rewritten as follows:

$$\frac{d^2T_{04}}{dt^2} + d_{04}^2T_{04} = -c^2\left(a_{04}\sigma(t) + b_{04}\frac{d^2\sigma(t)}{dt^2}\right) \tag{41}$$

where, $a_{04}=-(12+kL^2/6EL)$, $b_{04}=-(L/6c^2E)$, and $d_{04}=c\sqrt{k}$. Eq. (41) can be rearranged further to obtain Eq. (42) as follows:

$$\left[\frac{d^2T_{04}}{dt^2} + c^2b_{04}\frac{d^2\sigma(t)}{dt^2}\right] + d_{04}^2\left[T_{04} + c^2b_{04}\sigma(t)\right] = -c^2a_{04}\sigma(t) + d_{04}^2c^2b_{04}\sigma(t) = \left(\frac{2c^2}{EL}\right)\sigma(t) \tag{42}$$

Eq. (42) can be written in a simplified manner to obtain Eq. (43) as follows:

$$\Rightarrow \frac{d^2m_4(t)}{dt^2} + d_{04}^2m_4(t) = f_4(t) \tag{43}$$

where,

$$m_4(t) = T_{04} + c^2b_{04}\sigma(t), \text{ and } f_4(t) = \left(\frac{2c^2}{EL}\right)\sigma(t) \tag{44}$$

We use Laplace transform to solve Eq. (43). Let us denote $L\{m_4(t)\}=M_4(s)$, and $L\{f_4(t)\}=F_4(s)$. Thus, we obtain

$$\begin{aligned} & s^2M_4(s)-sm_4(0)-\frac{dm_4(0)}{dt}+d_{04}^2M_4(s)=F_4(s) \\ & \Rightarrow M_4(s)=\left(\frac{s}{s^2+d_{04}^2}\right)m_4(0)+\left(\frac{1}{s^2+d_{04}^2}\right)\frac{dm_4(0)}{dt}+\left(\frac{1}{s^2+d_{04}^2}\right)F_4(s) \\ & \Rightarrow m_4(t)=m_4(0)\cos(d_{04}t)+\frac{dm_4(0)}{dt}\frac{\sin(d_{04}t)}{d_{04}}+\int_{\tau=0}^{t}\frac{1}{d_{04}}\sin(d_{04}(t-\tau))f_4(\tau)d\tau \end{aligned} \tag{45}$$

note that,

$$\begin{aligned} & m_4(0)=T_{04}(0)+c^2b_{04}\sigma(0)=\left(\frac{L}{6E}\right)\sigma(0)-\left(\frac{L}{6E}\right)\sigma(0)=0, \text{ and} \\ & \frac{dm_4(0)}{dt}=\frac{dT_{04}(0)}{dt}+c^2b_{04}\frac{d\sigma(0)}{dt}=\left(\frac{L}{6E}\right)\frac{d\sigma(0)}{dt}-\left(\frac{L}{6E}\right)\frac{d\sigma(0)}{dt}=0 \end{aligned} \tag{46}$$

and thus, using Eqs. (44)–(46), we finally obtain

$$T_{04}(t)=-c^2b_{04}\sigma(t)+\frac{2c^2}{ELd_{04}}\int_{\tau=0}^{t}\sigma(\tau)\sin(d_{04}(t-\tau))d\tau \tag{47}$$

Substituting the expressions T_{n4}, T_{04} obtained from Eqs. (40) to 47) into Eq. (29) and finally into Eq. (14), we finally get

$$u_4(x,t)=u_1(x,t)-u_2(x,t)=T_{04}(t)+\sum_{n\geq 1}T_{n4}(t)\cos\left(\frac{n\pi x}{L}\right)+\frac{\sigma(t)}{E}\left(\frac{x^2}{L}-x\right) \tag{48}$$

We now introduce another variable, $u_3\equiv u_3(x,t)$ which is defined as follows:

$$u_{\mathbf{3}}(x,t)=u_{\mathbf{1}}(x,t)+u_{\mathbf{2}}(x,t) \tag{49}$$

Additionally, we define $u_3\equiv u_3(x,t)$ in an alternative manner as follows:

$$u_{\mathbf{3}}(x,t)=r(x,t)+s(x,t) \tag{50}$$

where $s(x,t)$ represents a smoothing function satisfying only the boundary conditions, i.e.,

$$\left.\frac{\partial s}{\partial x}\right|_{(0,t)}=\frac{\sigma(t)}{E} \tag{51}$$

$$\left.\frac{\partial s}{\partial x}\right|_{(L,t)}=\frac{\sigma(t)}{E} \tag{52}$$

Adding Eqs. (3) and (4), and substituting Eq. (50), we obtain another governing differential equation of the system, given by

$$\frac{\partial^2 r}{\partial x^2}-\frac{1}{c^2}\frac{\partial^2 r}{\partial t^2}=-\frac{\partial^2 s}{\partial x^2}+\frac{1}{c^2}\frac{\partial^2 s}{\partial t^2} \tag{53}$$

subjected to boundary conditions and initial conditions, given by Eqs. (54)–(57), respectively.

$$\left.\frac{\partial r}{\partial x}\right|_{(0,t)}=0 \tag{54}$$

$$\left.\frac{\partial r}{\partial x}\right|_{(L,t)}=0 \tag{55}$$

$$r(x,0)=-s(x,0) \tag{56}$$

$$\left.\frac{\partial r}{\partial t}\right|_{(x,0)}=-\left.\frac{\partial s}{\partial t}\right|_{(x,0)} \tag{57}$$

Since boundary conditions are to be satisfied, choice of $s(x,t)$ is made on the basis of Neumann boundary conditions, and is thus represented by

$$s(x,t)=\frac{x\sigma(t)}{E} \tag{58}$$

Substituting Eq. (58) into right-hand side of Eq. (53), we thus have the following differential equation of the system, given by

$$\frac{\partial^2 r}{\partial x^2}-\frac{1}{c^2}\frac{\partial^2 r}{\partial t^2}=p_3(x,t)=p_{03}(t)+\sum_{n\geq 1}p_{n3}(t)\cos\left(\frac{n\pi x}{L}\right) \tag{59}$$

where,

$$p_3(x,t) = \frac{x}{c^2 E}\frac{d^2\sigma(t)}{dt^2} \tag{60}$$

$$p_{03}(t) = \frac{1}{L}\int_{x=0}^{L} p_3(x,t)dx = \left(\frac{L}{2c^2E}\right)\frac{d^2\sigma(t)}{dt^2} \tag{61}$$

$$p_{n3}(t) = \frac{2}{L}\int_{x=0}^{L} p_3(x,t)\cos\left(\frac{n\pi x}{L}\right)dx = \left(\frac{2L}{c^2E}\right)\left(\frac{\cos(n\pi)-1}{n^2\pi^2}\right)\frac{d^2\sigma(t)}{dt^2} \tag{62}$$

Assume, $r(x,t)=X_3(x)T_3(t)$. The Eigen values and functions are thus given by

$$\lambda_{n3} = \left(\frac{n\pi}{L}\right)^2, \quad n \geq 0 \tag{63}$$

$$X_{n3}(x) = \cos\left(\frac{n\pi x}{L}\right), \quad n \geq 0 \tag{64}$$

Hence, the formal solution of the problem is given by formal Fourier series, as

$$r(x,t) = \sum_{n\geq 0} T_{n3}(t)\cos\left(\frac{n\pi x}{L}\right) = T_{03}(t) + \sum_{n\geq 1} T_{n3}(t)\cos\left(\frac{n\pi x}{L}\right) \tag{65}$$

Substituting Eq. (65) into left-hand side of Eq. (59) and equating both sides, we get

$$\frac{d^2T_{n3}}{dt^2} + \left(\frac{n\pi c}{L}\right)^2 T_{n3} = -c^2 p_{n3}(t), \quad n \geq 1 \tag{66}$$

$$\frac{d^2T_{03}}{dt^2} = -c^2 p_{03}(t) \tag{67}$$

The initial conditions, Eqs. (56) and (57), can be rewritten as follows:

$$\begin{aligned} & r(x,0) = T_{03}(0) + \sum_{n\geq 1} T_{n3}(0)\cos\left(\frac{n\pi x}{L}\right) = -s(x,0) = -\frac{x\sigma(0)}{E} \\ & \Rightarrow T_{03}(0) = -\frac{L\sigma(0)}{2E}, \; T_{n3}(0) = -\frac{2L\sigma(0)}{E}\left(\frac{\cos(n\pi)-1}{n^2\pi^2}\right) \end{aligned} \tag{68}$$

$$\begin{aligned} & \left.\frac{\partial r}{\partial t}\right|_{(x,0)} = \frac{dT_{03}(0)}{dt} + \sum_{n\geq 1}\frac{dT_{n3}(0)}{dt}\cos\left(\frac{n\pi x}{L}\right) = -\left.\frac{\partial s}{\partial t}\right|_{(x,0)} = -\frac{x}{E}\frac{d\sigma(0)}{dt} = q_3(x) = q_{03} + \sum_{n\geq 1} q_{n3}\cos\left(\frac{n\pi x}{L}\right) \\ & \Rightarrow \frac{dT_{03}(0)}{dt} = q_{03} = \frac{1}{L}\int_{x=0}^{L} q_3(x)dx = -\frac{L}{2E}\frac{d\sigma(0)}{dt}, \quad \text{and} \\ & \Rightarrow \frac{dT_{n3}(0)}{dt} = q_{n3} = \frac{2}{L}\int_{x=0}^{L} q_3(x)\cos\left(\frac{n\pi x}{L}\right)dx = -\frac{2L}{E}\left(\frac{\cos(n\pi)-1}{\pi^2 n^2}\right)\frac{d\sigma(0)}{dt}, \quad n \geq 1 \end{aligned} \tag{69}$$

Eq. (66) can be rewritten as follows:

$$\frac{d^2T_{n3}}{dt^2} + e_{n3}^2 T_{n3} = -c^2 a_{n3}\frac{d^2\sigma(t)}{dt^2}, \quad n \geq 1 \tag{70}$$

where, $a_{n3} = (2L/c^2E)(\cos(n\pi)-1/n^2\pi^2)$, and $e_{n3}=(n\pi c/L)$. Eq. (70) can be rearranged further to obtain Eq. (71) as follows:

$$\left[\frac{d^2T_{n3}}{dt^2} + c^2 a_{n3}\frac{d^2\sigma(t)}{dt^2}\right] + e_{n3}^2\left[T_{n3} + c^2 a_{n3}\sigma(t)\right] = e_{n3}^2 c^2 a_{n3}\sigma(t), \quad n \geq 1 \tag{71}$$

Eq. (71) can be written in a simplified manner to obtain Eq. (72) as follows:

$$\Rightarrow \frac{d^2y_3(t)}{dt^2} + e_{n3}^2 y_3(t) = g_3(t) \tag{72}$$

where,

$$y_3(t) = T_{n3} + c^2 a_{n3}\sigma(t), \text{ and } g_3(t) = e_{n3}^2 c^2 a_{n3}\sigma(t) \tag{73}$$

We use Laplace transform to solve Eq. (72). Let us denote $L\{y_3(t)\}=Y_3(s)$, and $L\{g_3(t)\}=G_3(s)$. Thus, we obtain

$$\begin{aligned} & s^2 Y_3(s) - s y_3(0) - \frac{dy_3(0)}{dt} + e_{n3}^2 Y_3(s) = G_3(s) \\ & \Rightarrow Y_3(s) = \left(\frac{s}{s^2+e_{n3}^2}\right)y_3(0) + \left(\frac{1}{s^2+e_{n3}^2}\right)\frac{dy_3(0)}{dt} + \left(\frac{1}{s^2+e_{n3}^2}\right)G_3(s) \end{aligned}$$

$$\Rightarrow y_3(t) = y_3(0)\cos(e_{n3}t) + \frac{dy_3(0)}{dt}\frac{\sin(e_{n3}t)}{e_{n3}} + \int_{\tau=0}^{t} \frac{1}{e_{n4}} \sin(e_{n3}(t-\tau)) g_3(\tau) d\tau \tag{74}$$

Note that,

$$y_3(0) = T_{n3}(0) + c^2 a_{n3}\sigma(0) = -\frac{2L\sigma(0)}{E}\left(\frac{\cos(n\pi)-1}{n^2\pi^2}\right) + \frac{2L\sigma(0)}{E}\left(\frac{\cos(n\pi)-1}{n^2\pi^2}\right) = 0, \text{ and}$$
$$\frac{dy_3(0)}{dt} = \frac{dT_{n3}(0)}{dt} + c^2 a_{n3}\frac{d\sigma(0)}{dt} = -\frac{2L}{E}\left(\frac{\cos(n\pi)-1}{n^2\pi^2}\right)\frac{d\sigma(0)}{dt} + \frac{2L}{E}\left(\frac{\cos(n\pi)-1}{n^2\pi^2}\right)\frac{d\sigma(0)}{dt} = 0 \tag{75}$$

and thus, using Eqs. (73)–(75), we finally obtain

$$T_{n3}(t) = -c^2 a_{n3}\sigma(t) + e_{n3}c^2 a_{n3}\int_{\tau=0}^{t} \sigma(\tau)\sin(e_{n3}(t-\tau))d\tau, \quad n \geq 1 \tag{76}$$

Lets us now solve Eq. (67). We proceed as follows. Eq. (67) can be rewritten as follows:

$$\frac{d^2T_{03}}{dt^2} = -c^2 a_{03}\frac{d^2\sigma(t)}{dt^2} \tag{77}$$

where, $a_{03} = (L/2c^2E)$. Eq. (77) can be rearranged further to obtain Eq. (78) as follows:

$$\left[\frac{d^2T_{03}}{dt^2} + c^2 a_{03}\frac{d^2\sigma(t)}{dt^2}\right] = 0 \tag{78}$$

Eq. (78) can be written in a simplified manner to obtain Eq. (79) as follows:

$$\Rightarrow \frac{d^2 m_3(t)}{dt^2} = 0 \tag{79}$$

where,

$$m_3(t) = T_{03} + c^2 b_{03} s(t) \tag{80}$$

We use Laplace transform to solve Eq. (79). Let us denote $L\{m_3(t)\} = M_3(s)$. Thus, we obtain

$$s^2 M_3(s) - s m_3(0) - \frac{dm_3(0)}{dt} = 0 \Rightarrow M_3(s) = \left(\frac{1}{s}\right)m_3(0) + \left(\frac{1}{s^2}\right)\frac{dm_3(0)}{dt} \Rightarrow m_3(t) = m_3(0) + t\frac{dm_3(0)}{dt} \tag{81}$$

Note that,

$$m_3(0) = T_{03}(0) + c^2 a_{03}\sigma(0) = -\left(\frac{L}{2E}\right)\sigma(0) + \left(\frac{L}{2E}\right)\sigma(0) = 0, \text{ and}$$
$$\frac{dm_3(0)}{dt} = \frac{dT_{03}(0)}{dt} + c^2 a_{03}\frac{d\sigma(0)}{dt} = -\left(\frac{L}{2E}\right)\frac{d\sigma(0)}{dt} + \left(\frac{L}{2E}\right)\frac{d\sigma(0)}{dt} = 0 \tag{82}$$

and thus, using Eqs. (80)–(82), we finally obtain

$$T_{03}(t) = -c^2 a_{03} s(t) \tag{83}$$

Substituting the expressions T_{n3}, T_{03} obtained from Eqs. (76) and (83) into Eq. (65) and then into Eq. (50), we finally get

$$u_3(x,t) = u_1(x,t) + u_2(x,t) = T_{03}(t) + \sum_{n \geq 1} T_{n3}(t)\cos\left(\frac{n\pi x}{L}\right) + \frac{x\sigma(t)}{E} \tag{84}$$

Thus, we have

$$u_1(x,t) = \frac{u_3(x,t) + u_4(x,t)}{2}, \quad \text{and} \quad u_2(x,t) = \frac{u_3(x,t) - u_4(x,t)}{2} \tag{85}$$

3. Results and discussion

As mentioned earlier, the current formulation has been derived with respect to any arbitrary pulse loading. In SHPB experiments, obtained loading pulses typically exhibit either triangular $\sigma(t) = (\sigma_{\max}/t_a)t$ or, half-sinusoidal $\sigma(t) = \sigma_{\max}\sin(\pi t/2t_a)$ waveforms. Both type of loading pulses were applied to the staggered composite. As per the formulation carried out by Wei et al. (2012), under quasi-static loading conditions, shearing stress at the ends of the overlap ($\tau_{\max}$) is given in terms of the maximum applied stress (σ_0) as follows:

$$\tau_{\max} = \tau|_{x=0} = \tau|_{x=L} = \frac{\sigma_0 b}{2}\sqrt{\frac{2G}{Ebh}}\coth\left(\frac{L}{2}\sqrt{\frac{2G}{Ebh}}\right) \tag{86}$$

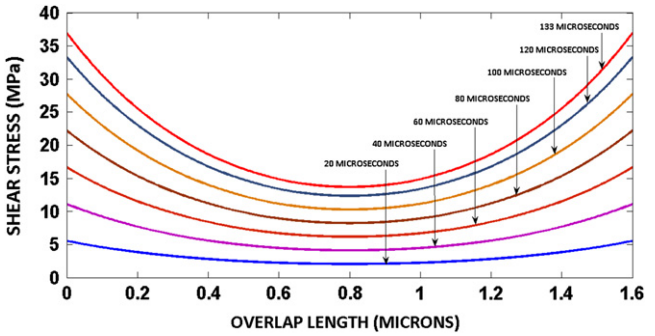

Fig. 2. Shear stress distribution profile over the overlap length at varying times under the application of triangular loading pulse.

Substitution of the geometrical and material properties of nacre (Barthelat et al., 2007b; Espinosa et al., 2011; Meyers et al., 2008; Jackson et al., 1988) into Eq. (85), results in $\sigma_0 = 133$ MPa. In order to visualize the variation of shear strength in the joint throughout the overlap length and over time, a maximum stress ($\sigma_{\max}$) of 133 MPa is hence applied and the time taken to attain this stress level (t_a) is chosen to be 133 μs. Shear stress distribution profiles obtained were almost identical corresponding to both types of loading. Fig. 2. shows the shear stress distribution profile. As it can be seen from Fig. 2, the shear stresses are maximum at the either ends of the overlap. With progressing time, sliding between the ceramic bricks continues to increase and thereby, shear stress at the ends continues to increase along with increasing stress levels toward the center of the joint. Indeed similar behavior has been observed under quasi-static loading conditions (Wei et al., 2012) as well as under finite element (FE) simulations (Sen et al., 2011) which justifies the efficacy of the analytical model.

Biological composite structures such as nacre, bone, etc. exhibit a generic microstructure (brick and mortar) at their most elementary level of architecture (Gao et al., 2003) where inorganic reinforcements serve as the load bearing member and the organic matrix mediates the load between adjacent ceramic bricks via shear. Under impact loading conditions, the total time for the event is in the order of tens of microseconds. Experimental studies (Sen et al., 2011) on adhesively bonded lap-joints account shearing failure of the adhesive as the predominant mode of failure under high-strain rate loading. Therefore, optimization of overlap length to provide maximum shearing resistance (at the ends) under dynamic loading conditions is a decisive parameter in the evolution of shells. Once the inorganic and organic constituents are fixed, nature cleverly chooses a characteristic overlap length such that shearing stress is a minimum and is thus, below or at par with the shear strength of the organic matrix. In order to prove this hypotheses, three natural materials were chosen (nacreous layer in abalone shell, spider silk and collagen in tendon/bone) and their characteristic overlap length scales were predicted based on this hypothesis. Figs. 3–5. identifies those critical overlap length scales for nacreous layer in abalone shell, spider silk and collagen in tendon/bone, respectively.

In nacre, microscopic observations (Meyers et al., 2008) reveals the existence of 0.5 μm ($\equiv 2b$) thick aragonite bricks bonded together by 25 nm ($\equiv h$) thick organic matrix and, an average overlap length of 1.6 μm (Barthelat et al., 2007b; Espinosa et al., 2011). The Young's modulus of elasticity ($\equiv E$) of the aragonite bricks is chosen to be 105.39 GPa and the shear modulus of the biopolymer matrix ($\equiv G$) is approximately 1.4 GPa (Wei et al., 2012). As it can be seen from Fig. 3(a), shear stress at the ends is minimum for an overlap length of ~2.5 μm. Note that the predicted value is reasonably close to the value observed in nature and that predicted by critical length scales (Wei et al., 2012) (of approximately 1.69 μm) under quasi-static loading scenario. Additionally, this critical overlap length remains constant even under increasing rates of loading as shown in Fig. 3(b) and clearly justifies why this particular overlap length is chosen by nature once the material parameters (E, G) and geometrical parameters (b, h) are fixed. Also, note that shear stress distribution profile, as shown in Fig. 2, was developed for an overlap length of 1.6 μm and interestingly, the maximum shear stress at the extremities at the end of the event matches exactly with the average shear strength of the polymer ($\equiv 37$ MPa) (Jackson et al., 1988), which justifies the choice of this overlap length by nacreous layer corresponding to time-dependent loading event.

Next the analytical model is applied to identify the critical overlap length between β-sheets in spider silk, the constituents of which are in nanometer scale levels. The building blocks for spider silk fibrils are β-sheets. Molecular dynamic simulations (Keten and Buehler, 2008; Keten et al., 2010) report an elastic modulus ($\equiv E$) of approximately 22.6 GPa, and shear modulus ($\equiv G$), which is representative of the crosslinking between b-sheets, of 4.6 GPa. β-sheet has a thickness ($\equiv 2b$) of about 1 nm, and the distance between β-sheets (equal to the length of H-bond), is approximately 0.3 nm ($\equiv h$). Experimental studies have revealed β-sheet length in the range from 2 nm to 8 nm (Penel et al., 2003). Once again, substitution of these values predicts the critical overlap length of ~5 nm (shown in Fig. 4) for dynamic loading event, which is in good agreement with experimental data. Additionally, the observed value is also in close agreement with those obtained by Wei et al. (2012) (≈ 5.7 nm) in their analyses under quasi-static loading conditions.

Finally, we apply the analytical model to identify the critical overlap length of collagen fibrils in tendon/bone. Experiments on tropocollagen molecules (Sun et al., 2002) reveal a wide distribution of elastic modulus ranging from

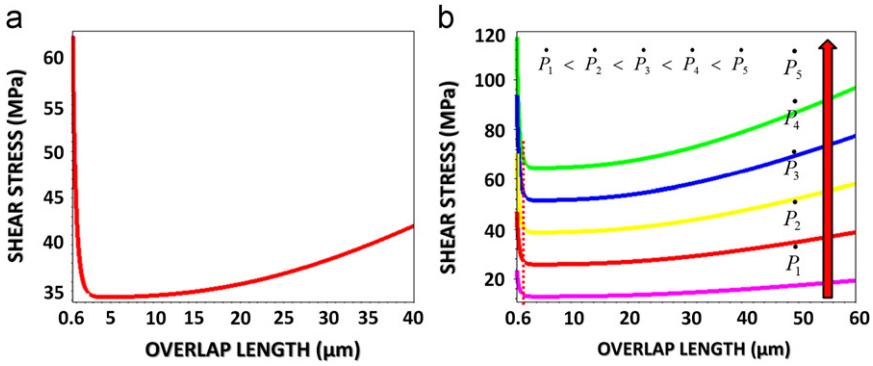

Fig. 3. Variation of shear stress at the extremities of the joint against overlap length for nacre (a), and its dependence on loading rate (b).

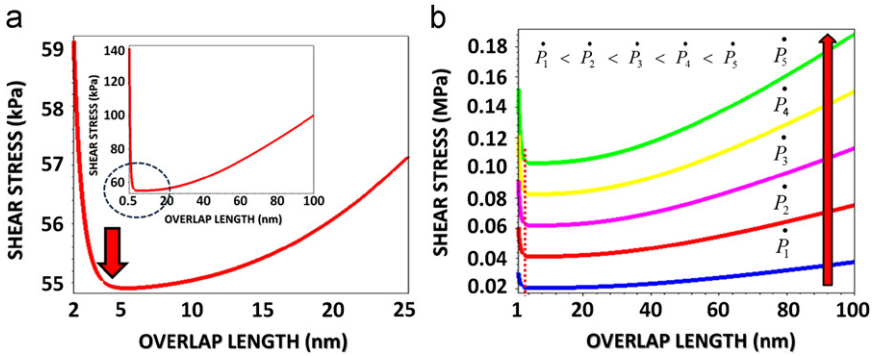

Fig. 4. Variation of shear stress at the extremities of the joint against overlap length for spider-silk (a), and its dependence on loading rate (b).

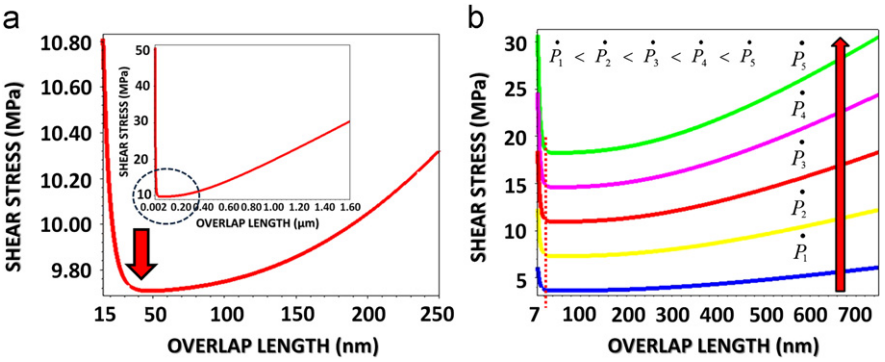

Fig. 5. Variation of shear stress at the extremities of the joint against overlap length for collagen in tendon/bone (a), and its dependence on loading rate (b).

0.35 GPa to 18 GPa has been attributed probably to varied strain rates used in the studies. An elastic moduli ($\equiv E$) of approximately 1 GPa was chosen for the tropocollagen molecule corresponding to the current scenario. For wet environmental conditions, over the overlap length, crosslinking shear modulus ($\equiv G$) in collagen fibrils was chosen to be approximately 3.4 MPa following measurements by micromechanical bending (Yang et al., 2008). Tropocollagen molecule has a diameter ($\equiv 2b$) of about 1.23 nm, and intra-tropocollagen molecular gap ($\equiv h$) is about 0.24 nm (Landis et al., 1993). Electron microscopy 3-D reconstruction technique identifies an overlap length of 27 nm (Landis et al., 1993). Substitution of the above mechanical and geometrical parameters into the analytical model predicts the critical overlap length of $\sim$36 nm (shown in Fig. 5) for dynamic loading event, which once again is in close agreement with experimental data and also in close agreement with those obtained for characteristic length scales ($\approx$31 nm) (Wei et al., 2012) under quasi-static loading conditions.

Next, we utilize our analytical model to predict the joint strength of an aluminum-Loctite adhesively bonded lap joint under impact loading conditions. Experiments, using SHPB, were carried out under high rates of loading for these lap joint

specimens (Sen et al., 2011). In order to predict the joint strength we proceeded as follows:

$$\varepsilon_x = \left.\frac{\partial u_1}{\partial x}\right|_{(L,t_f)} \tag{87}$$

$$v_x(L,t_f) = v_t \Rightarrow \varepsilon_t = \left(\frac{c}{c_t}\right)\varepsilon_x \Rightarrow \sigma_{predicted} = \frac{A_b E_b \varepsilon_t}{A_{ls}} \tag{88}$$

where, c, c_t represent stress-wave velocity in the aluminum, and wave velocity through the transmission bar (Aluminum alloy 7075), respectively. Transmitted strain is calculated on the basis of velocity compatibility condition at the specimen transmission bar interface. A_b, A_{ls} represent the cross-sectional area of the transmission bar, and area of the adhesive lap joint, respectively. E_b, t_f denotes the Young's modulus of elasticity of the transmission bar and failure time of adhesively bonded lap joint. Table 1 lists the predicted joint strength against experimentally measured data and they are found to be in reasonably close agreement with each other. Based on this observation, the efficacy of our analytical model can be validated.

Thus, once the material properties and geometrical parameters are fixed, choice of overlap length can be based upon the essence of minimization of shear stress at the extremities to promote maximum load transfer by polymer via shear and to withstand the entire dynamic event. Too far a deviation from the optimal length will raise shear stress at the ends appreciably, which will in-turn will result in premature failure of the joint (will not be able to withstand the whole incident pulse) and thereby, reduce joint efficiency. Thus, perspectives drawn from this point-of-view can be utilized as a vital design guideline in tailoring adhesively bonded single lap composite joints (at micro/meso/macro scales). Note that, the current observations are based on triangular pulse loading. However, similar set of observations are encountered if a half-sinusoidal pulse loading is applied, and for brevity purposes are not discussed here.

Based on fracture mechanics concepts, Gao et al. (2003) postulated the adoption of nanometer sized inorganic reinforcements in order to achieve a state of flaw-intolerance. Presence of nanometer sized inorganic crystals can be visualized from another point-of-view. Shear transfer efficiency of staggered architectural composites can be qualitatively interpreted by consideration of elastic strain-energy density via shear transfer mechanism. The effective strain, ε_{eff}, and the effective stress, σ_{eff}, can be written as

$$\varepsilon_{eff} \equiv \left.\lim_{t\to t_a}\frac{2u_1}{L}\right|_{(L,t)} \tag{89}$$

$$\frac{\sigma_{eff}(x,t) = \lim_{t\to t_a} b\sigma(t) - \rho b(L-x)\ddot{u}_1\big|_{avg}}{(2b+h)} \tag{90}$$

and the elastic strain energy density, w_{eff}, is thus given by

$$w_{eff} = \int \sigma d\varepsilon = \frac{1}{2}\sigma_{eff}\varepsilon_{eff} \tag{91}$$

for triangular loading pulse loading. Similar to our previous analyses, once the material properties and geometrical parameters are fixed, w_{eff} becomes a function of overlap length (L). A plot of elastic strain energy density variation against overlap length is shown in Fig. 6(a). As it can be seen from Fig. 6(a), as the length of the overlap decreases and reaches nanoscale dimensions, elastic strain energy density of the staggered composite increases. Note that, the plot in Fig. 6(a) corresponds to dimensions and properties for nacreous layer in seashell. In fact, this phenomena has been observed

Table 1
Comparison of experimentally measured joint strength against those predicted by analytical model for varying overlap area and loading rates.

Loading rate (kN/μs)	$\sigma_{Maximum}$ (MPa)	t_f (μs)	Overlap length (mm)	Overlap area (mm^2)	$\sigma_{Experimental}$ (MPa)	$\sigma_{Predicted}$ (MPa)
0.64	27.68	12	10	158.75	34.62	33.78
	37.77	24			47.24	40.44
1.08	40.51	16	10	158.75	50.67	49.44
	38.22	18			47.80	46.64
0.87	41.08	16	10	158.75	36.29	35.38
	38.22	12			47.51	46.32
	38.22	18			34.91	34.03
0.65	21.22	12	15	238.5	17.67	17.22
	25.67	18			21.37	20.83
	30.76	20			25.61	24.96
1.08	43.59	13	15	238.5	36.29	35.38
	57.07	18			47.51	46.32
	41.94	20			34.91	34.03
1.52	72.42	16	15	238.5	60.29	58.77
	66.04	16			54.98	53.59

$E=71.7$ GPa, $G=1.2$ GPa, $h=0.5$ mm, $2b=15.9$ mm.

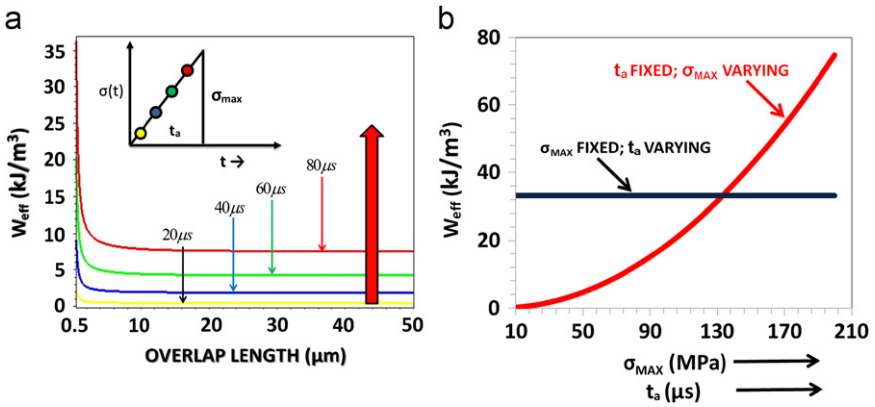

Fig. 6. Variation of elastic strain energy density against varying overlap length at different intervals of time under the application of triangular pulse loading (a), and dependence of elastic strain energy density on loading rate, under the application of triangular pulse loading, shown via (1) varying max stress (keeping time at maximum stress fixed)-shown in red and (2) varying time at max stress (keeping maximum stress fixed)-shown in black; dependence of w_{eff} is markedly pronounced towards increasing stress-levels than for time under the application of triangular pulse loading.

experimentally (for macro-scale specimens) where for a given loading rate, joint-strength increases with decreasing overlapping area (Sen et al., 2011). It has been observed that the toughening rate (tearing modulus) in bone is higher than in nacre (Wang and Gupta, 2011), which can be inferred from Fig. 6(a). and attributed to the presence of nanometer sized building blocks in its staggered architecture. This explains why nature chooses nano-sub-micrometer scale overlapping feature for biocomposite structural integrity.

One of the other interesting outcomes of the current analytical model is that as the loading rate increases, the elastic strain energy density (w_{eff}) of the staggered composite increases as well. As it can be seen from Fig. 6(b), dependence of w_{eff} is markedly pronounced towards increasing stress-levels than for time rise of the loading pulse. Thus, staggered composites showed increasing energy absorption behavior with increasing loading-rates and thereby, exhibit dynamic self-stiffening behavior (Huang et al., 2011). This aspect of self-stiffening behavior under impact loading conditions will find particular relevance in application of these types of composites as protective materials under impact.

Note that, based on the current model, we can also explain the reason as to why the dynamic compressive strength of abalone nacre is nearly 50% higher than its static counterpart, as observed from SHPB experiments by Menig et al. (2000) and Huang et al. (2011). As was postulated by Gao et al. (2003), Gao (2006), under quasi-static conditions, nature uses, particularly, aspect ratio of the mineral crystals to promote strain amplification mechanism and thereby obtain an optimal balance for deformation in organic and inorganic components to obtain maximum potential. de Gennes and Okumura (2000) and Okumura and de Gennes (2001) presented an analytical solution for a layered system, based on laminar architecture of the seashells, and accounted the existence of weaker stress concentration ahead of the crack tip in these materials in comparison to traditional isotropic elastic materials, under quasi-static loading conditions. In our current investigation, we have attempted to establish a link between superior strength of nacre, under impact loading conditions for a given loading-rate, and its microstructural dependence, via the existence of an optimum overlap length during shear-transfer. The loading rates applied for dynamic compression testing (Menig et al., (2000)) of abalone nacre varied from 15 GPa s^{-1} to 25 GPa s^{-1}. Corresponding to loading rates of 15 GPa s^{-1}, 20 GPa s^{-1} and, 25 GPa s^{-1}, the current analytical model predicts an effective strain of 0.0070, 0.0090, and 0.0117, respectively, which are in reasonable agreement with the experimentally observed values of 0.008, 0.0095, and 0.0145, respectively, obtained by Menig et al. (2000). Additionally, the predicted maximum compressive strength is approximately 450 MPa which is again in reasonable agreement with experimentally obtained strengths of nearly 500 MPa (Menig et al., 2000; Huang et al., 2011). Predicted shear strains corresponding to loading rates of 15 GPa s^{-1}, 20 GPa s^{-1} and, 25 GPa s^{-1} were 0.178, 0.237, and 0.297, respectively, which is less than experimentally obtained maximum shear strains of approximately 0.45 (Menig et al., 2000). This accounts for the reason as to why staggered architecture composites exhibit elevated compressive strength under time-dependent loading conditions. Additionally, under the current model, the elastic strain energy density (w_{eff}) will thereby turn out to be higher for dynamic loading than for quasi-static loading conditions, which can explain the reason for superior damage tolerance of staggered architecture composites. The outcome of the current research will thus provide beneficial guidelines in custom-design manufacture of hybrid bio-inspired protective composite materials.

Ji and Gao (2004, 2010) and Ji (2008) had analyzed the staggered arrangement of the biological structure previously under quasi-static loading conditions. They postulated that under quasi-static conditions, two parameters play a significant role: (a) presence of nanometer-sized crystals to obtain a state of maximum flaw tolerance and, (b) presence of an optimum aspect ratio of the mineral crystals to promote strain amplification mechanism and thereby obtain an optimal balance for deformation in organic and inorganic components to obtain maximum potential. Apart from visualizing the design in staggered architecture materials from optimal overlap length point of view, the current model

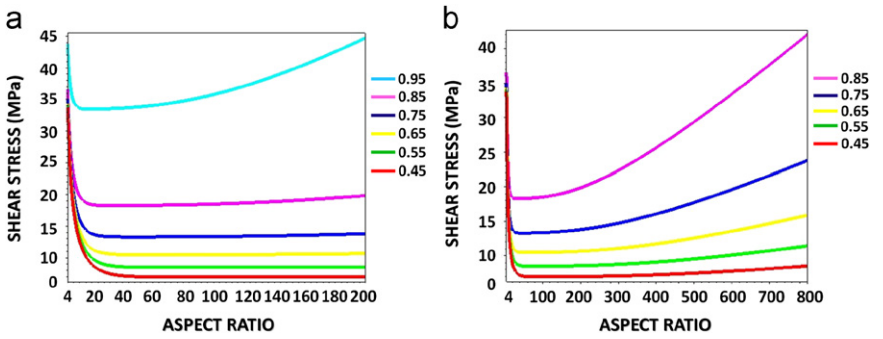

Fig. 7. Plot showing the dependence of maximum shear stress (at the ends of overlap) as a function of aspect ratio and volume fraction of the ceramic bricks for: aspect ratio varying between 4 and 200 (a) and, 4 and 800 (b) under the application of triangular pulse loading, corresponding to a given loading-rate.

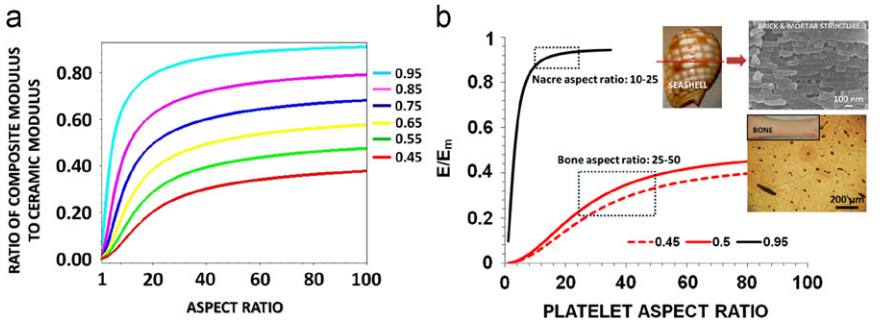

Fig. 8. Plot showing the dependence of the ratio of composite modulus to Young's modulus of the ceramic bricks for varying aspect ratio and volume fraction of the ceramic bricks: correlation between dynamic (a) and quasi-static (b) regime, corresponding to a given loading rate.

can also be visualized from aspect ratio and volume fraction of the ceramic point of view, for a given thickness of the ceramic brick.

Under time-dependent loading conditions, optimum aspect ratios exist for varying volume fractions of ceramic in staggered architecture materials, as shown in Fig. 7((a) and (b)). For lower volume fractions of the ceramic, a wide range of optimal aspect ratio exists which would correspond to maximum load transfer capability of the joint via attainment of a state of minimum shear. For example, bone and dentin comprise of plate-like crystals having aspect ratio varying from 25 to 50 and a volume fraction of 0.40–0.55 (Ji and Gao, 2004). For very high volume fraction of the ceramic, the range of aspect ratio available to obtain a state of minimum shear is narrow, as shown in Fig. 7(a). Similarly, nacre comprises of ceramic bricks having an aspect ratio varying from 10 to 16 and a volume fraction of nearly 0.95 (Ji and Gao, 2004). In order to obtain a more clearer understanding of the interdependence of aspect ratio, volume fraction of the ceramic, and constituent material properties under impact loading conditions, a plot of ratio of composite modulus to the ceramic Young's modulus as a function of aspect ratio and volume fraction is shown in Fig. 8(a) and (b) shows the dependence obtained under quasi-static conditions using the tension-shear-chain (TSC) model as was postulated by Ji and Gao (2004).

It should be noted that extensive literature exists quantifying role of microstructure and material parameters on the behavior of staggered architecture, however under quasi-static loading conditions. Note that, in our current investigations, what we are trying to establish is that staggered architecture in biological composites is designed in such a unique manner that the structure would be able to provide maximum resistance both under quasi-static loading conditions, and when subjected to severe dynamic loads when attacked by predators (as resistance to shell crushing is an integral part of shell evolution process).

3.1. *Limitations of the analytical model and future directions*

Formulation of the model is laid on the foundation of linear elastic material behavior only, i.e., the stresses are linearly dependent on strain only (via material properties E, G which are considered constant); however, the organic matrix being a visco-elastic material, under dynamic loading conditions, strain-rate ($\dot{\varepsilon}_s$) of the organic matrix is expected to play a key role in load transfer via shear. Incorporation of strain-rate ($\dot{\varepsilon}_s$) dependent terms and large-scale deformation aspects would help in understanding mechanical behavior of these composites under very high-strain rate loading; for example under blast loading conditions. Additionally, incorporation of plastic behavior of the intermediate matrix is also expected to contribute to the cause. This could possibly account for the difference obtained between experimentally observed and

theoretically predicted overlap length values in nacre as shown previously. Work is in progress in this direction. To further and better understand this aspect, the model can be extended to include strain-rate dependence and large-scale deformation of the intermediate polymer, effect of alignment (regular, stairwise, random), number of hierarchical levels, etc. These can be identified as future directions of the current work. Additionally, the current model is restricted to the scenario where adherends are made of same materials. Work is in progress to understand the behavior of staggered architecture composites where adherends are made of dissimilar materials.

Under static loading conditions, characteristic lengths predicted were essentially based on (a) stress transfer point of view, $L^* = \sqrt{2Ebh/G}$, as was postulated by Chen et al. (2009) and, (b) an optimization on both strength and toughness fronts, $L^* = 2.318\sqrt{Ebh/G}$, as postulated by Wei et al. (2012). Under dynamic rates of loading, the shear stress developed at the interface is also a function of the overlap length (L). If a joint has to withstand the entire dynamic event, critical overlap length exists based on the essence of minimization of shear stress at the extremities to promote maximum load transfer capability by polymer via shear (once the material properties and geometrical parameters are fixed). Thereby, in order to obtain optimum joint efficiency, an optimal overlap length is evaluated as follows:

$$L_{\text{optimal}} \equiv \text{Minimize}[\tau(x,t)]_L = \text{Minimize}\left[\tfrac{G}{h} \times u_4(x,t)\right]_L = \\ = \text{Minimize}\left[\frac{G}{h} \times \left\{ \begin{array}{l} \frac{\sigma(t)L}{6E} + \frac{2c^2}{ELd_{04}} \int_{\tau=0}^{t} \sigma(\tau)\, \sin(d_{04}(t-\tau))d\tau \\ + \sum\limits_{n \geq 1} \left\{ \begin{array}{l} -\frac{2L}{E}\left(\frac{1+\cos(n\pi)}{n^2\pi^2}\right)\sigma(t) + \\ \frac{2c}{E}\left(\frac{1+\cos(n\pi)}{\sqrt{kL^2+n^2\pi^2}}\right) \int_{\tau=0}^{t} \sigma(\tau)\, \sin\left(c\sqrt{k+\left(\frac{n\pi}{L}\right)^2}(t-\tau)\right)d\tau \end{array} \right\} \\ \cos\left(\frac{n\pi x}{L}\right) \\ + \frac{\sigma(t)}{E}\left(\frac{x^2}{L} - x\right) \end{array} \right\}\right]_L \tag{92}$$

It is to be noted that there does not exist a direct relationship between dynamic overlap length and static overlap length. This can be better addressed with reference to the figure shown below.

Under static loading conditions, the shear stress (at the extremities of the interface) (Wei et al., 2012) as given by the equation below, decreases till a critical value is attained and remains constant thereafter.

$$\tau_{static}\big|_{x=(0,\frac{L}{2})} = \frac{\sigma b\lambda}{2\sin h\left(\frac{\lambda L}{2}\right)} \cosh\left(\frac{\lambda L}{2}\right); \quad \lambda = \sqrt{\frac{2G}{Ebh}} \tag{93}$$

On the contrary, it can be clearly seen (Fig. 9) that critical overlap length exists under dynamic rates of loading, and thus addresses the vitality of optimal overlap length under dynamic rates of loading.

Under quasi-static loading conditions, choice of critical overlap length in staggered biocomposites attempts to optimize mechanical performance on both strength and toughness fronts. However under impact loading conditions, since shear transfer mechanism is the most versatile parameter, choice of critical overlap length is mainly directed towards minimization of peak shear stresses at the extremities of the joint. However, nature simultaneously addresses the nano-sub-micro overlap length scales in an attempt to improve on toughness perspective as well. This feature can be adapted as an important guideline in the design of adhesively bonded lap joints, gradient microstructural composites, etc. under dynamic rates of loading. The outcome of the current research will thus provide beneficial guidelines in custom-design manufacture of hybrid bio-inspired protective composite materials.

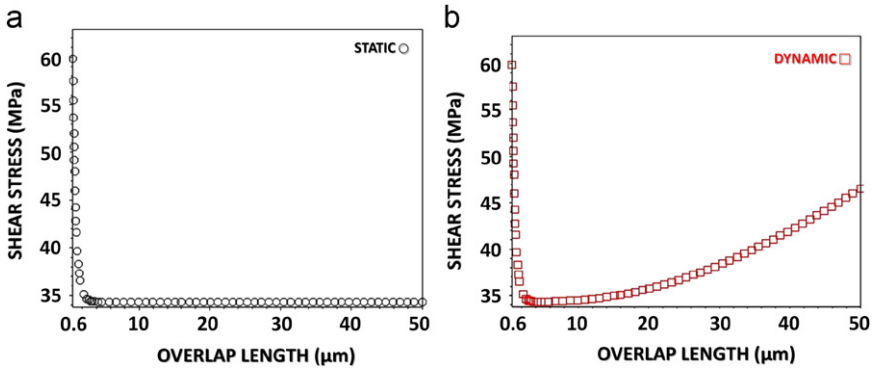

Fig. 9. Variation of shear stress at the interface as a function of overlap length in a material (in the current case, nacreous layer in seashells) under (a) static and (b) dynamic rates of loading.

4. Conclusions

In our current investigation, we have addressed the following aspects with regards to materials exhibiting staggered microstructure as its most elementary level of architecture under impact loading conditions, by considering a triangular loading pulse: (1) Identifying the structure-property correlationship for these materials, (2) existence of a critical overlap length which optimizes load transfer mechanism between the adjacent reinforcements, (3) ratify the choice of nanometer building blocks in biological composites under time-dependent loading, (4) generalizing the application of the concept to the case of macro-scale adhesively bonded lap joints, (5) explaining the reason behind superior damage tolerance and elevated dynamic compressive strength of nacre, and (6) theoretically justify the applicability of staggered microstructural composites under impact loading conditions. The outcome of the current research will provide beneficial guidelines in custom-design manufacture of hybrid bio-inspired protective composite materials.

Author contributions

Conception and organization of the current work: Abhishek Dutta and Srinivasan Arjun Tekalur; Analytical model development & solution: Abhishek Dutta, Milan Miklavcic and Srinivasan Arjun Tekalur; Analysis of results: Abhishek Dutta and Srinivasan Arjun Tekalur; Manuscript draft: Abhishek Dutta and Srinivasan Arjun Tekalur.

Acknowledgement

Research was sponsored by the Army Research Laboratory and was accomplished under Cooperative Agreement Number W911NF-08-2-0059.

References

Barthelat, F., Espinosa, H.D., 2007a. An experimental investigation of deformation and fracture of nacre-mother of pearl. Exp. Mech. 47, 311–324.
Barthelat, F., Tang, H., Zavattieri, P., Li, C.M., Espinosa, H., 2007b. On the mechanics of mother-of-pearl: a key feature in the material hierarchical structure. J. Mech. Phys. Solids 55, 306–337.
Chen, B., Wu, P.D., Gao, H., 2009. A characteristic length for stress transfer in the nanostructure of biological composites. Compos. Sci. Technol. 69, 1160–1164.
de Gennes, P.G., Okumura, K., 2000. On the toughness of biocomposites. C. R. Acad. Sci. Paris, 257–261. t.1, Ser. IV.
Evans, A., Suo, Z., Wang, R., Aksay, I., He, M., Hutchinson, J., 2001. Model for the robust mechanical behavior of nacre. J. Mater. Res. 16, 2475–2484.
Espinosa, H.D., Juster, A.L., Latourte, F.J., Loh, O.Y., Gregoire, D., Zavattieri, P.D., 2011. Tablet-level origin of toughening in abalone shells and translation to synthetic composite materials. Nat. Commun. 2, 173.
Gao, H., Ji, B., Jäger, I., Arzt, E., Fratzl, P., 2003. Materials become insensitive to flaws at nanoscale: lessons from nature. Proc. Nat. Acad. Sci. U.S.A. 100, 5597–5600.
Gao, H., 2006. Application of fracture mechanics concepts to hierarchical biomechanics of bone and bone-like materials. Int. J. Fract. 138, 107–137.
Hulmes, D.J.S., Wess, T.J., Prockop, D.J., Fratzl, P., 1995. Radial packing, order and disorder in collagen fibrils. Biophys. J. 68, 1661–1670.
Huang, Z., Li, H., Pan, Z., Wei, Q., Chao, Y.J., Li, X., 2011. Uncovering high-strain rate protection mechanism in nacre. Sci. Rep. 1, 148, http://dx.doi.org/10.1038/srep00148.
Jackson, A.P., Vincent, J.F.V., Turner, R.M., 1988. The mechanical design of nacre. P. R. Soc. London B 234, 415–440.
Jager, I., Fratzl, P., 2000. Mineralized collagen fibrils: a mechanical model with a staggered arrangement of mineral particles. Biophys. J. 79, 1737–1746.
Ji, H., Gao, H., 2004. Mechanical properties of nanostructure of biological materials. J. Mech. Phys. Solids 52, 1963–1990.
Ji, B.H., 2008. A study of the interface strength between protein and mineral in biological materials. J. Biomech. 41, 259–266.
Ji, B., Gao, H., 2010. Mechanical principles of biological nanocomposites. Annu. Rev. Mater. Res. 40, 77–100.
Kessler, H., Ballarini, R., Mullen, R.L., Kuhn, L.T., Heuer, A.H., 1996. A biomimetic example of brittle toughening: (I) Steady state multiple cracking. Comput. Mater. Sci. 5, 157–166.
Kamat, S., Su, X., Ballarini, R., Heuer, A.H., 2000. Structural basis for the fracture toughness of the shell of the conch Strombus gigas. Nature 405, 1036–1040.
Kotha, S.P., Kotha, S., Guzelsu, N., 2000. A shear-lag model to account for interaction effects between inclusions in composites reinforced with rectangular platelets. Compos. Sci. Technol. 60, 2147–2158.
Katti, K.S., Katti, D.R., Pradhan, S.M., Bhosle, A., 2005. Platelet interlocks are the key to toughness and strength in nacre. J. Mater. Res. 20, 1097–1110.
Keten, S., Buehler, M.J., 2008. Asymptotic strength limit of hydrogen-bond assemblies in proteins at vanishing pulling rates. Phys. Rev. Lett. 100, 198301.
Keten, S., Xu, Z., Ihle, B., Buehler, M.J., 2010. Nanoconfinement controls stiffness, strength and mechanical toughness of—sheet crystals in silk. Nat. Mater. 9, 359–367.
Landis, W., Song, M., Leith, A., McEwen, L., McEwen, B., 1993. Mineral and organic matrix interaction in normally calcifying tendon visualized in three dimensions by high-voltage electron microscopic tomography and graphic image reconstruction. J. Struct. Biol. 110, 39–54.
Landis, W.J., 1995. The strength of a calcified tissue depends in part on the molecular structure and organization of its constituent mineral crystals in their organic matrix. Bone 16, 533–544.
Liu, G., Ji, B.H., Hwang, K.C., Khoo, B.C., 2011. Analytical solutions of the displacement and stress fields of the nanocomposite structure of biological materials. Compos. Sci. Technol. 71, 1190–1195.
Menig, R., Meyers, M.H., Meyers, M.A., Vecchio, K.S., 2000. Quasi-static and dynamic mechanical response of Haliotis rufescens (abalone) shells. Acta Mater. 48, 2383–2398.
Menig, R., Meyers, M.H., Meyers, M.A., Vecchio, K.S., 2001. Quasi-static and dynamic mechanical response of Strombus gigas (conch) shells. Mater. Sci. Eng., A 297, 203–211.
Meyers, M., Lin, A., Chen, P., Muyco, J., 2008. Mechanical strength of abalone nacre: role of the soft organic layer. J. Mech. Behav. Biomed. Mater. 1, 76–85.
Okumura, K., de Gennes, P.-G., 2001. Why is nacre strong?: elastic theory and fracture mechanics for biocomposites with stratified structures. Eur. Phys. J. E 4, 121–127.
Penel, S., Morrison, R.G., Dobson, P.D., Mortishire Smith, R.J., Doig, A.J., 2003. Length preferences and periodicity in strands. Antiparallel edge sheets are more likely to finish in non hydrogen bonded rings. Protein Eng. 16, 957.

Sarikaya, M., Gunnison, K.E., Yasrebi, M., Aksay, J.A., 1990. Mechanical propertymicrostructural relationships in abalone shell. Mater. Res. Soc. 174, 109–116.
Sun, Y.L., Luo, Z.P., Fertala, A., An, K.N., 2002. Direct quantification of the flexibility of type I collagen monomer. Biochem. Biophys. Res. Commun. 295, 382–386.
Song, F., Soh, A., Bai, Y., 2003. Structural and mechanical properties of the organic matrix layers of nacre. Biomaterials 24, 3623–3631.
Shuchun, Z., Yueguang, W., 2007. Effective elastic modulus of bone-like hierarchical materials. Acta Mech. Solida Sin. 20, 198–205.
Sen, O., Tekalur, S.A., Jilek, C., 2011. The determination of dynamic strength of single lap joints using the split Hopkinson pressure bar. Int. J. Adhes. Adhes. 31, 541–549.
Volkersen, O., 1938. Die Nietkraftverteilung in zugbeanspruchten Nietverbindungen mit konstanten Laschenquerschnitten. Luftfahrtforsch 15, 41.
Veis, A., Sabsay, B., 1987. The collagen of mineralized matrices. In: Peck, W.A. (Ed.), Bone and Mineral Research/5. Elsevier Science Publications, New York, Amsterdam, Tokyo, pp. 1–63.
Wagner, H.D., Weiner, S., 1992. On the relationship between the microstructure of bone and its mechanical stiffness. J. Biomech. 25, 1311–1320.
Wang, R., Suo, Z., Evans, A., Yao, N., Aksay, I., 2001. Deformation mechanisms in nacre. J. Mater. Res. 16, 2485–2493.
Wang, R., Gupta, H.S., 2011. Deformation and fracture mechanisms of bone and nacre. Annu. Rev. Mater. Res. 41, 41–73.
Wei, X., Naraghi, M., Espinosa, H.D., 2012. Optimal length scales emerging from shear load transfer in natural materials: application to carbon-based nanocomposite design. ACS Nano 6 (3), 2333–2344.
Yang, L., Van Der Werf, K.O., Fitié, C.F.C., Bennink, M.L., Dijkstra, P.J., Feijen, J., 2008. Mechanical properties of native and cross-linked type I Collagen fibrils. Biophys. J. 94, 2204–2211.
Zhang, Z.Q., Liu, B., Huang, Y., Hwang, K.C., Gao, H., 2010. Mechanical properties of unidirectional nanocomposites with non-uniformly/randomly staggered platelet distribution. J. Mech. Phys. Solids 58, 1646–1660.
Zhang, Z., Zhang, Y.-W, Gao, H., 2011. On optimal hierarchy of load-bearing biological materials. Proc. R. Soc. B 278, 519–525.